High-throughput whole-brain mapping of rhesus monkey at micron resolution

Fang Xu[1,2,12], Yan Shen[3,12], Lufeng Ding[3,12], Chao-Yu Yang[3,12], Heng Tan[4,5], Hao Wang[1,6], Qingyuan Zhu[1], Rui Xu[7], Fengyi Wu[2], Cheng Xu[1], Qianwei Li[1], Peng Su[8], Li I. Zhang[9], Hongwei Dong[10], Robert Desimone[7], Fuqiang Xu[2,8,11], Xintian Hu[4,11], Pak-Ming Lau[3,6,*], Guo-Qiang Bi[1,2,6,11,*]

[1]Center for Integrative Imaging, Hefei National Laboratory for Physical Sciences at the Microscale, and School of Life Sciences, University of Science and Technology of China, Hefei, Anhui, China

[2]CAS Key Laboratory of Brain Connectome and Manipulation, Interdisciplinary Center for Brain Information, The Brain Cognition and Brain Disease Institute, Shenzhen Institutes of Advanced Technology, Chinese Academy of Sciences; Shenzhen-Hong Kong Institute of Brain Science-Shenzhen Fundamental Research Institutions, Shenzhen, Guangdong, China

[3]CAS Key Laboratory of Brain Function and Disease, and School of Life Sciences, University of Science and Technology of China, Hefei, Anhui, China

[4]Key Laboratory of Animal Models and Human Disease Mechanism, Kunming Institute of Zoology, Chinese Academy of Sciences, Kunming, Yunnan, China

[5]Department of Pathology and Pathophysiology, Kunming Medical University, Kunming, Yunnan, China

[6]Institute of Artificial Intelligence, Hefei Comprehensive National Science Center, Hefei, Anhui, China

23   [7]McGovern Institute for Brain Research, Massachusetts Institute of Technology,

24   Cambridge, Massachusetts, USA

25   [8]State Key Laboratory of Magnetic Resonance and Atomic and Molecular Physics, Key

26   Laboratory of Magnetic Resonance in Biological Systems, Wuhan Institute of Physics

27   and Mathematics, Chinese Academy of Sciences, Wuhan, Hubei, China

28   [9]Zilkha Neurogenetic Institute, Center for Neural Circuits & Sensory Processing

29   Disorders, Keck School of Medicine, University of Southern California, Los Angeles,

30   California, USA

31   [10]USC Stevens Neuroimaging and Informatics Institute, Laboratory of Neuro Imaging

32   (LONI), Keck School of Medicine of University of Southern California, Los Angeles,

33   California, USA

34   [11]CAS Center for Excellence in Brain Science and Intelligence Technology, Shanghai,

35   China

36   [12]These authors contributed equally

37   [*]Correspondence: gqbi@ustc.edu.cn (G.-Q.B.), plau@ustc.edu.cn. (P.-M.L.)

38

Abstract

40   Whole-brain mesoscale mapping of primates has been hindered by large brain size and

41   the relatively low throughput of available microscopy methods. Here, we present an

42   integrative approach that combines primate-optimized tissue sectioning and clearing with

43   ultrahigh-speed, large-scale, volumetric fluorescence microscopy, capable of completing

44   whole-brain imaging of a rhesus monkey at 1 μm × 1 μm × 2.5 μm voxel resolution within

45   100 hours. A progressive strategy is developed for high-efficiency, long-range tracing of

46   individual axonal fibers through the dataset of hundreds of terabytes, establishing a

47   "Serial sectioning and clearing, 3-dimensional Microscopy, with semi-Automated

48   Reconstruction and Tracing" (SMART) pipeline. This system supports effective

49   connectome-scale mapping of large primates that reveals distinct features of

50   thalamocortical projections of the rhesus monkey brain at the level of individual axonal

51   fibers.

52   **Introduction**

53   Given the status of the rhesus macaque (*Macaca mulatta*) as a major experimental

54   animal for modeling human cognitive functions and brain diseases [1,2], a fundamental

55   task in neuroscience and neurology is mapping structural connectivity among different

56   brain regions and neurons (*i.e.*, the mesoscopic connectome) of the monkey brain [3,4], as

57   those established for the mouse brain [5,6]. Connectivity mapping of non-human primate

58   brains has to date relied primarily on bulk labeling of specific brain regions with

59   anterograde and retrograde tracers, followed by interleaved 2D imaging of serial thin

60   sections [7-9]. However, this approach is tedious and lacks the continuity necessary for

61   tracking individual axons throughout the brain.

62 Widely used tractography approaches based on diffusion-weighted magnetic resonance

63 imaging (dMRI) are able to image the entire monkey or human brain as a whole, but

64 their anatomical accuracy is inherently limited [10-12]. Light-sheet microscopy (LSM)

65 combined with whole-brain clearing techniques can image intact mouse brains, but lacks

66 the resolution to distinguish individual axons [13-17]. Recently developed block-face

67 imaging techniques, including fluorescent micro-optical sectioning tomography (fMOST)

68 [18] and serial two-photon (STP) tomography [19], have successfully implemented brain-wide

69 axonal tracing in mice, and have opened a new era of connectomic mapping [20, 21].

70 However, given that these techniques require several days to image a mouse brain, it is

71 impractical to scale up these methods toward systematic connectomic mapping for

72 macaque or human brains.

73 To break these technical bottlenecks, we developed an integrative approach consisting

74 of serial sectioning of the brain tissue into thick slices, clearing with primate-optimized

75 uniform clearing solutions, microscopic imaging using ultrafast volumetric on-the-fly

76 scanning, and a semi-automated process for volume reconstruction and axonal tracing.

77 This "SMART" strategy and pipeline (Fig. 1a), owing to ultra-high speed and scalability,

78 overcame several key technical challenges to enable high-resolution mapping of the

79 entire macaque brain. In a proof-of-principle experiment, we generated a projection map

80 from viral-labeled thalamic neurons to the cerebral cortex and unveiled distinct axonal

81 routing patterns in the folded banks along the superior temporal sulcus (*sts*), and carried

82 out efficient semi-automated tracing of neuronal fibers through the near petabyte dataset

83 of the monkey brain.

84 **Results**

85 **Serial sectioning, clearing and high-throughput imaging of the macaque brain**

86 The first major challenge for imaging large brains is sample preparation. The difficulty of

87 reagent penetration increases exponentially with tissue thickness, making it exceedingly

88 difficult to achieve uniform histological staining or clearing of the whole monkey brain,

89 which is more than 200 times larger than a mouse brain (Fig. 1b) [8]. We therefore chose

90 to section the brain into slices before subsequent clearing and imaging. A robust

91 workflow was established with hydrogel-based embedding to minimize tissue loss and

92 distortion during sectioning and clearing (Supplementary Figs. 1 and 2; online Methods).

93 A macaque brain was sectioned into about 250 consecutive 300-μm slices which were

94 treated with a primate-optimized uniform clearing method (PuClear) that combines Triton

95 X-100-based gentle membrane permeabilization with high refractive index matching (Fig.

96 1c). Unlike the widely used sodium dodecyl sulfate (SDS)-based clearing methods such

97 as CLARITY [13, 14] that we found inadequate for imaging clearly through the white matter

98 (WM) of primate tissue, PuClear has a refractive index of 1.52, yielding uniform

99 transparency through the full depth of 300-μm slices including WM areas (Fig. 1d, top

100 panels). Importantly, PuClear preserves the morphology of neurons labeled by Nissl

101 stain (Fig. 1d, bottom panels) and showed excellent compatibility for both

102 immunostaining and retrograde tracing using cholera toxin subunit B (CTB)

103 (Supplementary Figs. 3 and 4).

104 Uniform clearing of thick brain slices also allowed us to overcome a second major

105 challenge, the long duration of time required for imaging a large brain at high resolution.

106 For this, we developed a new iteration of our recently reported synchronized on-the-fly-

107 scan and readout (VISoR) technique [22]. This improved "VISoR2" system is optimized for

108   ultrahigh-speed volumetric imaging of the larger monkey brain sections (Fig. 1e).

109   Besides instrumental upgrades including long-travel linear stages and a more compact

110   and stable light-path, the new system was implemented with an optimized control

111   sequence for the sCMOS camera, the illumination laser, and the galvanometer scanner

112   (Supplementary Fig. 5; online Methods).

113   We achieved 250 Hz blur-free imaging of a 0.7×2 mm^2 field of view containing the optical

114   section of the slice with smooth stage movement at any speed ranging from 0.5 to 20

115   mm/s. This configuration corresponds to a voxel resolution of 1.0×1.0×(1.4~56) μm^3 and

116   a continuous data rate of 400 million voxels per second (Supplementary Fig. 5;

117   Supplementary Video 1). Thus the system is capable of imaging a mouse brain that is

118   serially sectioned, cleared and mounted on a single glass slide within 30 min at 1.0 μm ×

119   1.0 μm × 2.5 μm resolution. Consequently, the collection of ~80 million single-channel

120   images (2048 × 788 pixels each) for all slices from one macaque brain only took 94

121   hours imaging time. This VISoR2-based imaging across three channels resulted in 750

122   terabytes of data for a rhesus macaque brain that was labeled via co-injection of AAV

123   cocktails mixed by an adeno-associated virus (AAV) carrying Cre recombinase and

124   another AAV carrying Cre-dependent fluorescent proteins (FPs) reporter, either eGFP or

125   mCherry, into the left and right superior colliculus (SC), respectively.

126   **Reconstruction of the entire macaque brain**

127   While the VISoR2 microscopy with significantly improved imaging speed overcame the

128   second challenge in primate brain mapping, it generated a third challenge: the analysis

129   of such large dataset. Available tools have been effective in handling terabyte-level

130   multi-tile images, but these tools cannot be used for non-overlapped image tiles [23, 24], or

131   lack automation for multi-hundred terabyte data [25]. We therefore developed a custom

132   software tool that implements automated volume stitching (Fig. 1f, Supplementary Fig.

133   6), including rigid-transformation-based 3D intra-slice stitching (Fig. 1g) and non-rigid-

134   transformation-based inter-slice alignment (Fig. 1h, Supplementary Video 2). Attesting

135   the strong performance of this tool, we found that the intra-slice stitching errors were ~2

136   μm for each axis (Fig. 1i) and the inter-slice alignment error of AAV labeled axons was

137   ~8 μm (Fig. 1j). Importantly, tissue loss between consecutively sectioned slices was

138   insignificant, as seen in the precise alignment of truncated cell bodies and axonal

139   branches (Fig. 1k). As we demonstrate below, this precision was sufficient for visually

140   tracing axonal projections. In practice, we reconstructed the whole brain at a coarse

141   voxel resolution ($10 \times 10 \times 10$ μm^3) to obtain an overview of brain structures, and also

142   established a robust transformation framework for on-demand reconstruction of user-

143   specified regions of interest (ROIs) at full resolution for detailed analysis of axonal

144   projections (Fig. 1l-n, and Supplementary Fig. 7).

145   **Mesoscopic mapping of thalamocortical projection**

146   To demonstrate the capacity of our system for mesoscopic mapping of neuronal

147   projections across the entire monkey brain, we bilaterally injected AAV cocktails into the

148   left and right medial dorsal nucleus of the thalamus (MD), with minor leakage to nearby

149   areas (Supplementary Fig. 8). The MD is known to generate dense projections to the

150   prefrontal cortex (PFC) [26, 27]. VISoR2 imaging and 3D reconstruction of this monkey

151   brain allowed for visualization of the global distribution of axons originating from the

152   injection sites and projecting to the cerebral cortex (Fig. 2a). From the 3D volume and a

153   series of virtual sections, it was clear that bundled fibers from the injection sites traveled

154   through the internal capsule in horizontal, obliquely lateral, and upward directions (Fig.

155   2b, Supplementary Video 3), before continuing on towards the frontal lobe, where they

156   primarily targeted the posterior orbitofrontal area (OFC) (Fig. 2c, Supplementary Fig. 9),

157   largely consistent with previous reports of the MD projections [26, 28]. Furthermore, the

158   resolution of the original images was sufficient for us to visualize individual axons and

159   branches, and to distinguish whether the fibers were passing by or making terminal

160   arborizations. For instance, our PFC mapping revealed that labeled axons terminate in

161   layer III and layer IV (Fig. 2d).Besides the canonical target areas of the MD in the

162   ipsilateral PFC with high-density arborizations of labeled axons, we also observed

163   various lower density, yet significant, fiber branches and arborizations in other areas

164   such as the ipsilateral secondary somatosensory cortex (SII) (Fig. 2e,f), which is known

165   to be a target of the ventral posterior inferior nucleus (VPI) and ventral posterolateral

166   nucleus (VPL) [29], and the temporal lobe, including superior temporal sulcus (*sts*) dorsal

167   (TPO) and ventral (TEa) bank areas (Fig. 2e,g-h, Supplementary Fig. 9). All projection

168   targets observed in this animal are summarized in Supplementary Table 1 and

169   visualized in Fig. 2i in a cortical map after flattening (Supplementary Fig. 10). Thus, the

170   high resolution and sensitivity of SMART imaging may help reveal previously unidentified

171   cortical targets of the MD, although some of these observations could be due to

172   inadvertent labeling of neurons in other nuclei close to the injection sites. More precise

173   injection or a sparse labeling approach that allows complete single neuron tracing will

174   help resolve such uncertainties and unveil detailed thalamocortical projection maps.

175   **SMART reveals distinct axonal routing strategies in local cortical folds**

176   The resolution of our system also allowed for identification of fine features of individual

177   axons in the projection sites where the fibers were not excessively dense. As an

178   example, we reconstructed a full-resolution volume of the areas near the *sts* and traced

179   30 randomly selected axonal segments (Fig. 3a,b and Supplementary Video 4) using

180   custom tracing software. Intriguingly, in these folded areas, the axons projecting to

181   layers III/IV of the TEa typically navigated to the dorsal side first, before separating into

182   two major groups: one group made sharp turns in the WM (Fig. 3c, top panel), traveling

183   along the boundary of the WM (Fig. 3c, bottom panel); the other group made right-angle

184   turns and traveled through the superficial cortical layers (Fig. 3d). We observed 4 distinct

185   classes of turning patterns for these axons (Fig. 3e-h). Such differences in the micro-

186   organization of these afferent axons may underlie their functional diversity, especially

187   when they make putative *en route* connections with different sets of neurons positioned

188   within various local circuits.

189   **Brain-wide axonal tracing of macaque neurons**

190   With the capacity of resolving individual axons, we set out to trace the long-range,

191   whole-brain projections of macaque axons but encountered yet another challenge.

192   Whereas convenient tools have been developed for brain-wide tracing of individual

193   axons in mouse [20, 30-32], it is computationally challenging to scale up these tools to handle

194   the whole brain volume of a macaque at full resolution. In addition, the reconstructed

195   local image is often of somewhat lower quality than the raw image, partly because of

196   errors introduced by non-linear deformation and interpolation steps that are implemented

197   to achieve global consistency. Therefore, we developed a computationally efficient

198   strategy for progressively tracing axons in blocks directly from raw images. For this, we

199   first generated a relatively low resolution ($10 \times 10 \times 10 \ \mu m^3$) reconstruction volume of

200   the macaque brain, and established a "SMART positioning system" (SPS) that employs

201   a set of bidirectional transformations to enable mapping between the initially defined

202   whole-brain coordinate system and the corresponding data from each raw image (Fig.

203   4a).

204   An iterative workflow was then established to trace the relatively sparsely labeled axons

205   projecting to the contralateral hemisphere (Fig. 4b). In this scheme, bright fiber trunks

206   were first identified in the low-resolution whole-brain image, followed by semi-automatic

207   tracing in full-resolution raw image blocks that were dynamically loaded as tracing

208   progressed along the axon track; this process proceeded until reaching the injection site

209   (where the fibers were too dense) (Fig. 4c) or reaching the nerve ending of each axonal

210   branch (Fig. 4d,e). When necessary, any misalignment between adjacent slices from

211   errors in the automatic registration process was manually corrected based on the

212   continuity of foreground neuronal fibers and background microvasculature

213   (Supplementary Fig. 11).

214   Using this progressive SMART tracing strategy, we tracked all 28 randomly selected

215   bright fiber trunks retrogradely back into the injection site and anterogradely to their

216   branching points. These fibers travel in parallel in a bundle within the internal capsule

217   before branching out into divergent cortical areas (Supplementary Fig. 12; distances

218   before branching: 26.8±1.6 mm; n=28). We also selected 6 from those fiber trunks and

219   mapped out their full terminal arborizations (Fig. 4f and Supplementary Video 5). For

220   tracing each axon, only 1.7±0.5 % of raw images were sequentially accessed (total size

221   of raw images: 238 TB; size of images accessed during tracing: 4.1±1.2 TB; n=6), with

222   multiple 600 MB image blocks (2048×788×200 voxels each) loaded into the memory at

223   each time, a workload manageable by a personal computer. Notably, most of these

224   axonal fibers form clustered arborizations in confined cortical regions, with negligible

225   subcortical arborizations (3.4±2.6 % of total axonal length; n=6), in striking contrast to

226   the previously mapped mouse thalamic projections from the MD and nearby reunions

227   nucleus (RE) (Supplementary Fig. 13; Supplementary Table 2).

228   **Discussion**

229   Owing to its implementation of optimized tissue slicing and clearing, ultrahigh-speed

230   imaging techniques, and efficient analysis tools for processing near-petabyte-scale

231   datasets, SMART bridges the gap in our understanding of functionally impactful

232   differences between rodent and human brain architectures, specifically by enabling the

233   efficient mapping of primate brains at subcellular resolution and supporting brain-wide,

234   long-range tracing of individual axons. Indeed, our proof-of-concept study has already

235   begun to reveal potential new targets of primate thalamocortical projections and to

236   highlight distinct properties of individual axons, including their long trunks and striking

237   turning patterns as they progress towards cortical targets. Although this initial study only

238   allowed for tracing of a small number of single fibers because of the very dense labeling

239   and relatively low throughput of semi-automatic axonal tracing, much sparser labeling is

240   achievable by lowering the concentration of Cre recombinase-carrying AAV in the viral

241   injection cocktail [33, 34], and combining with high-performance computing (HPC) and

242   automated tracing techniques, it is expected that the SMART system will allow for

243   mapping the full morphology of a potentially huge number of individual neurons [20, 30, 35],

244   thus paving the way toward a truly connectome-scale understanding of the primate

245   brain.

246   It should also be noted that SMART is compatible with widely used experimental

247   techniques for histological labeling, thereby supporting analysis of samples not

248   amenable to viral labeling, for example postmortem human brains [36]. The strategies

249   underlying SMART, including non-overlapped physical slicing and computational

250   stitching, high-throughput blur-free imaging, and progressive tracing in the raw image

251   stacks, are all readily scalable and applicable to other biological samples, including

252   internal organs and even the whole bodies of various species that labeled with antero- or

253   retrograde transneuronal transporting viruses [37]. Application of these techniques have

254   the potential to yield unprecedented understanding of brain architecture, and high-

255   precision, systems-level insights about the development, basic functions, and

256   neurological pathology of the entire nervous system.

257

258

259 **Methods**

260 **Labeling viruses**

261 For anterograde neural labeling, recombinant adeno-associated viruses (rAAVs) were

262 generated by transient triple transfection of HEK293 cells as previously reported [38]. Cap

263 serotype 9 was chosen to package the AAV vectors to achieve high transduction levels

264 and high titers (>10^{12} vg/mL). A strong promoter CAG and transcription control element

265 WPRE were chosen to construct pAAV-CAG-Dio-EGFP-WPRE-pA or pAAV-CAG-Dio-

266 mCherry-WPRE-pA constructs for stable fluorescent protein (FP) expression in primates

267 [39]. To increase neuronal specificity, we used the hSyn promoter to construct pAAV-

268 hSyn-Cre-WPRE-pA to serve as a controller of FP-expressing vectors.

269

270 **Mice**

271 Eight-week-old male C57BL/6 and Thy1-YFP-H (Jax: 003782) mice were used in this

272 study for prototyping the sample preparation and imaging methods. All mice experiments

273 were carried out following protocols approved by the Institutional Animal Care and Use

274 Committees of the University of Science and Technology of China (USTC). All mice

275 used in this study were group-housed with a 12-hour light/dark cycle (lights on at 7 a.m.)

276 with free access to food and water.

277 4% hydrogel monomer solution (HMS) was prepared for perfusion by mixing 40% (w/v)

278 acrylamide (4% final concentration; V900845, Sigma), 2% (w/v) bisacrylamide (0.05%

279 final concentration; V3141, Promega), 10× phosphate buffer saline (PBS; 1× final

280 concentration; 70011044, ThermoFisher), 8% (w/v) paraformaldehyde (PFA; 4% final

281 concentration; 157-8, Electron Microscopy Sciences), distilled water, and VA-044

282 thermal initiator (0.25% final concentration; 223-02112, Wako) [13]. The perfusion

283   procedures were carried out following a modified protocol based on a previous study [22].

284   Mice were deeply anesthetized with 1% sodium pentobarbital solution, followed by

285   transcardial perfusion with 20 mL of 37°C PBS, 20 mL ice-cold PBS, and finally 20 mL of

286   ice-cold 4% HMS. All solutions were perfused at a uniform rate of 10 mL/min. Mouse

287   brains were harvested and immediately placed into 20 mL ice-cold 4% HMS and

288   incubated at 4°C for 24-48 h to allow further diffusion of the hydrogel monomers into the

289   tissue.

290

Monkeys

292   Three adult, 10-year-old, male rhesus macaques (*Macaca mulatta*) were used in this

293   study. Macaques were obtained from the breeding colonies of the Primate Research

294   Center of Kunming Institute of Zoology, Chinese Academy of Sciences (KIZ, CAS),

295   which was accredited by the Association for Assessment and Accreditation of Laboratory

296   Animal Care (AAALAC International). The experimental procedures were approved by

297   the Institutional Animal Care and Use Committee (IACUC) of KIZ, CAS (IACUC No.

298   IACUC18018).

299   In order to prevent gastric regurgitation caused by the anesthesia, fasting and water

300   deprivation were implemented for at least 6 h before surgery. Animals were anesthetized

301   using 10 mg/kg ketamine hydrochloride injection (i.m., 50 mg/mL, Zhong Mu Bei Kang

302   pharmaceutical industry limited company, China) and maintained with 20 mg/kg

303   pentobarbital sodium (i.m., 40 mg/mL, Merck, Germany). During the surgery, heart rate

304   and core temperature were monitored using a rectal probe and ECG monitor. MRI

305   assisted brain region positioning was used for accurate encephalic injection as

306   previously described [40]. MRI scanning was performed using a 3-T scanner (uMR770,

307   United Imaging, China) with a 12-channel knee coil. FP-expressing rAAVs (pAAV-CAG-

308   Dio-EGFP-WPRE-pA, 4.70×10^{12} vg/mL, 2 μL, for the left hemispheres, or pAAV-CAG-

309   Dio-mCherry-WPRE-pA, 3.15×10^{12} vg/mL, 2 μL, for the right hemispheres) and Cre-

310   expressing rAAVs (pAAV-hSyn-Cre-WPRE-pA, 2.09×10^{12} vg/mL, 2 μL) were mixed at a

311   1:1 ratio for each injection. In this study, a macaque was injected with these AAV

312   cocktails at both sides of the superior colliculus (SC, AP:-4 mm; ML: ±3 mm; DV:-38

313   mm) and another macaque was injected with these mixtures at both sides of the

314   mediodorsal nucleus (MD, AP: 1 mm; ML: ±3 mm; DV: -38 mm). A third monkey was

315   injected with a cholera toxin subunit B-Alexa Fluor 647 conjugate (CTB-AF647; C34778,

316   Invitrogen) at the quadrigeminal cistern. The duration of injection was more than 20

317   minutes (including 5 minutes each after inserting and before withdrawing the

318   microsyringe). Antibiotics were used for 3 d after surgery. Injection sites were further

319   confirmed from reconstructed whole-brain images.

320   Transcardial perfusions were carried out 8 weeks after surgery. Thirty min after

321   anesthesia, each animal was sequentially perfused with the following solutions at the

322   specified speed: PBS 8 L (37°C, 10 mL/s), PBS 1 L (4°C, 1.5 mL/s), 4% HMS 1L (4°C,

323   1.5 mL/s), and 4% HMS 1 L (4°C, 0.3 mL/s). The brains were extracted immediately

324   after perfusion within 30 min.

325

326   **Tissue embedding and slicing**

327   A post-fixation procedure with hydrogel was set up for crosslinking proteins and

328   minimizing tissue loss. Immediately after the macaque brain was excised, it was

329   immersed into 500 mL of 4% HMS and stored at 4°C for 1 week before embedding to

330   allow penetration of the fixatives. Then the brain was immersed in the embedding

331   solution, a 1:1 mixture of 4% HMS (2% final concentration) and 20% bovine serum

332   albumin (BSA; 10% final concentration; V900933, Sigma), incubated at 4°C for 1 week,

333   polymerized at 37°C for 4-5 h, and washed 3 times in PBS to remove residual reagents.

334   Embedding with the mixture of HMS and BSA provides not only *in situ* fixation of

335   proteins[13] , but also high material stiffness and toughness for preserving slice integrity

336   during sectioning (Supplementary Fig. 2). Embedded brains were sectioned into about

337   250 pieces of 300-μm-thick slices using a vibroslicer (Compresstome VF-800,

338   Precisionary Instruments). All slices of each brain were collected and each slice was

339   placed in a Petri dish with 40 mL PBS and stored at 4°C.

340

Sample clearing

341

342   The PuClear clearing method was established based on previously reported CLARITY

343   [13], CUBIC [17] techniques with optimization for primate brain tissues, consisting of

344   membrane permeabilization and refractive index (RI) matching. Brain slices were first

345   treated with a high concentration Triton X-100 solution (5% in PBS; T928, Sigma) for 3-4

346   d at 37°C with gentle shaking to adequately increase membrane permeability, and were

347   then washed with PBS 3 times. High refractive index (RI) solution was prepared by

348   mixing 50 wt% iohexol (29242990.99, Hisyn Pharmaceutical), 23 wt% urea (A600148-

349   0002, Sangon), 11 wt% 2,2',2",-nitrilotriethanol (V900257, Sigma), and 16 wt% distilled

350   water. The final refractive index of PuClear RI-matching solution is 1.52. Before imaging,

351   brain slices mounted onto the glass substrates were incubated in this solution for at least

352   1 h to allow the sample getting optically transparent.

353

Sample staining

354

355   Staining was performed after PuClear perforation and before mounting. For immuno-

356   labeling, membrane-perforated slices were placed into Petri dishes and immersed in

357   blocking solution (5% (w/v) BSA in 0.3% PBST) overnight. After that, samples were

358   incubated with the primary antibody in 0.3% PBST for 3-4 d followed by 3 washes with

359   PBS. Subsequently, samples were incubated with the secondary antibody in 0.3% PBST

360   for 2-3 d, followed by 3 times washing with PBS. Dishes were kept at 4°C during

361   blocking, staining, and washing with gentle shaking. For fluorescent Nissl staining, the

362   blocking step was skipped and the slices were incubated with NT640 in 0.3% PBST for

363   3-4 d at 37°C followed by washing 3 times with PBS. For DAPI staining, samples were

364   incubated with DAPI stock solution for 1 d at 37°C followed by washing 3 times with

365   PBS.

366   The following antibodies and dyes were used in this study (name, company, catalog

367   number, dilution): Polyclonal Rabbit Anti-Glial Fibrillary Acidic Protein (GFAP), Dako,

368   Z0334, 1:100; Anti-Tyrosince Hydroxylase Antibody, Milipore, MAB318, 1:500; Alexa

369   Fluor 647 AffiniPure Donkey Anti-Mouse IgG (H+L), Jackson ImmunoResearch

370   Laboratories, 715-605-151, 1:200; Alexa Fluor 488 AffiniPure Donkey Anti-Rabbit IgG

371   (H+L), Jackson ImmunoResearch Laboratories, 711-545-152, 1:200; NeuroTrace

372   640/660 Deep-Red Fluorescent Nissl Stain (NT640), ThermoFisher, N21483, 1:200;

373   DAPI, Beyotime, C1006, stock solution.

374

375   **VISoR2 microscope**

376   We designed and built the VISoR2 microscope based on the VISoR technique described

377   previously for mouse brain imaging [22], with long-range sample stages and major

378   upgrades for improving its stability, repeatability, as well as the practical imaging speed.

379   The microscope was equipped with four lasers with wavelengths of 405 nm, 488 nm,

380   552 nm, and 647 nm (all from Coherent). Incident light was combined and illuminated

381   onto a galvo scanner (GVS011, Thorlabs). The position of the scanner was in

382   conjugation with the back focal plane of an illumination objective (10X/NA 0.3, Olympus)

383   via two coupled relay lenses (F=150mm, Thorlabs). 1-D scanning of the scanner

384   generated an illuminating plane that was overlapped with the focal plane of an imaging

385   objective (10X/NA 0.3 or 20X/NA 0.5, both from Olympus). Emission light was filtered

386   with bandpass filters (450/50, 520/40, 600/50, and 700/50 for the four laser sources,

387   respectively; all from Semrock). Images were collected on a CMOS camera (Flash 4.0

388   v3, Hamamatsu) through a tube lens (IX2-TLU, Olympus) and a 0.63X adapter (TV0.63,

389   Olympus). The objectives were both positioned at a 45-degree incline to the samples. A

390   linear stage (DDSM100, Thorlabs) and a stepper stage (LTS150, Thorlabs) were used

391   for X- and Y-axis movements, respectively, and a stepper stage (MCZ20, Zaber) was

392   used for Z movement.

393   The devices were controlled by custom software written in C++. To maximize the

394   imaging throughput, the camera was aligned in the center of the light path and its

395   readout was bi-directional in an "*external trigger syncreadout*" mode. During imaging, the

396   X stage moved smoothly at a speed ranging from 0.5 mm/s to 20 mm/s for different

397   resolution requirements. To avoid blurring due to motion, we synchronized the lasers,

398   the scanner, the camera, and the stages with a DAQ board (NI PCIe-6374, National

399   Instruments). The Y-step size was set to include 10% overlapped regions between

400   adjacent image stacks.

401   Each time the X-stage finished accelerating and moved at a constant speed, it

402   generated a rising edge signal which triggered a timer in the DAQ board to start

403   signaling, continuously generating signals for lasers, the scanner, and the camera until

404   imaging was complete, resulting a stack of image frames of the 45-degree oblique

405   optical sections of the sample. 400 million voxels were acquired per second,

406   approaching the maximum data rate of the CMOS camera. Multi-color imaging was

407   implemented by sequentially imaging individual channels and computationally registering

408   all channels after all images were acquired.

409

Workstation

411   The image acquisition software was run on a workstation equipped with an Intel Xeon

412   E5-2680 CPU, an NVIDIA GTX 1060 graphics card, and 128 GB memory. It was

413   equipped with 2 disk arrays each consisting of 8 SSDs configured in RAID5 for

414   alternatively acquiring and transporting data to a remote petabyte storage server

415   connected via 10 Gbps fiber-optic intranet. Windows 10 Pro 64-bit operating system was

416   run on this workstation.

417

Data Management and Compression

419   The VISoR2 system acquired about 20,000 image frames for a typical monkey brain

420   slice, consisting of several image stacks, each generated during a one-way uniform

421   motion of the X stage. We adopted the BigTIFF format instead of standard TIFF to allow

422   storing all images of a slice into a single file sized ~200 GB with embedded OME-XML

423   metadata, adapted to the Bio-Formats plugin in ImageJ/Fiji [41, 42]. We also forked this

424   plugin to provide additional visualization features optimized to these large OME-TIFF

425   images (https://github.com/dinglufe/bioformats). A single-channel VISoR2 image volume

426   of a whole rhesus monkey brain contained ~1×10^{14} voxels of 16-bit depth which

427   occupies ~250 TB of storage. An efficient image compression method is necessary for

428   handling such a large dataset, which requires not only a high compression ratio but also

429   low computation resource consumption to compromise the heavy data load. We used

430   the lossless Lempel–Ziv–Welch (LZW) algorithm to compress the raw images [43, 44],

431   which typically reached a compression ratio of 2:1. Furthermore, we also used a slightly

432 lossy compression strategy by truncating the 4 least significant bits and performing a

433 proper rounding to the higher 12 bits of each 16-bit voxel value of the original images,

434 followed by additional LZW compression. This method practically reaches a

435 compression ratio of 8:1 with little computation time and CPU usage and worked in real-

436 time during image acquisition. The theoretical peak-signal-noise-ratio (PSNR) of this

437 method achieves 83.0, as determined by $PSNR = 20 * \log_{10}(\frac{MAX_I}{\sqrt{MSE}})$, where MAX_I equals

438 65535, the maximum possible voxel value of a 16-bit image, and MSE is the rounding

439 error, which was determined by $MSE = (8^2 + 2 * \sum_{i=1}^{7} i^2)/2^4 = 21.5$, supposing the

440 values of the lower 4 bits follow a uniform distribution. More importantly, this method is

441 seamlessly compatible with all visualization and analysis tools developed for TIFF

442 images.

443

444 **Automatic whole brain reconstruction**

445 The volume reconstruction was automatically performed by custom software written in

446 Python.

447 **Intra-slice stitching**. Raw images of a brain slice were organized as a set of image

448 stacks, with metadata of their physical positions recorded from the output of the X-, Y-,

449 and Z- stages. Then raw image substacks from the overlapped region of two adjacent

450 image stacks, each consisting of 100 continuous images, were sampled to calculate the

451 stitching translation between these two stacks. The stitching translation was determined

452 as the shift that minimized their normalized cross-correlation (NCC) in virtue of the open-

453 source tool *elastix* (http://elastix.isi.uu.nl). The stitched image stacks were then

454 generated by resampling raw images.

455   The precision of this intra-slice stitching method was calculated by evaluating the NCC

456   between small random ROIs cut from the overlapped regions of two stitched stacks, with

457   one stack fixed and the other moving in a 20 px × 20 px × 20 px window. The stitching

458   error was determined as the shift that minimized the NCC and was further refined

459   through quadratic interpolation of three points nearest to the NCC minimum and then

460   taking the sub-pixel location corresponding to the minimum of the quadratic curve. The

461   sub-pixel refinement formula is:

462
$$x_{subpixel\ min,i} = x_i + \frac{n_{x_i+1} - n_{x_i-1}}{4n_{x_i} - 2n_{x_i+1} - 2n_{x_i-1}}$$

463   where x_i is the i-th axis position of the minimal value in the NCC array, and n_{x_i} is the

464   NCC value at the position x_i.

465   **Channel alignment.** For calculating the precise displacement of each stack among

466   sequential multi-channel imaging, one of the channels (usually the eGFP channel) was

467   chosen as the reference channel and each other channel was aligned to the reference

468   channel stack by stack. Several pairs of image substacks consisting of 100 continuous

469   frames were sampled from both this channel and the reference channel at the edges of

470   the brain slices detected by a brightness threshold. The contours of the brain slices

471   provided autofluorescence features for computational alignment. The images were

472   filtered using a gradient magnitude filter, then the translation between each pair of image

473   substacks was calculated using the mutual information metric with *elastix*. The median

474   value of the translation calculated from all the pairs of image substacks was determined

475   as the displacement between this channel and the reference channel.

476   **Flattening.** The upper and lower surfaces of the brain slice in 3D images were identified

477   and digitally flattened in this step. The upper and lower surfaces were represented by

478   two images H_U and H_L. The value of $H_U(x, y)$ or $H_L(x, y)$ at any point (x, y) was defined as

479 the distance from the upper boundary of the 3D image to the upper or lower surface of

480 the brain slice, respectively. Numerically, H_U and H_L were determined based on the

481 optimization of 3 factors: (1) the value of the z-gradient image, which was generated by

482 convolving the stitched image with a z-gradient filter; (2) the Laplacian of H_U and H_L as a

483 smooth penalty of surface; (3) the distance between the upper and lower surfaces

484 compared to the thickness of the slice (i.e. 300 μm physical distance). With these

485 constraints, in the areas surrounding cortical sulci and ventricles, the boundaries of brain

486 slices detected by the gradient filter which were not real physical cuts were not

487 recognized as slice surfaces. The stitched slice image was then digitally resliced and

488 flattened by moving and scaling along the Z-direction for each pixel, assuming both the

489 upper and lower surfaces were horizontal, and the distance between any pair of $H_U(x, y)$

490 and $H_L(x, y)$ was 300 μm. The sets of H_U and H_L for all slices were used for further inter-

491 slice stitching and SPS positioning.

492 **Inter-slice stitching.** Adjacent slices were stitched together after flattening by

493 registering the upper surfaces of the *n*-th slice and the lower surfaces of the (*n-1*)-th

494 slice. The registration was performed by *elastix*, using metrics of *mutual information* and

495 *rigidity penalty*. The deformation field of surfaces was globally optimized using the

496 stochastic gradient descent (SGD) algorithm, by minimizing the average deformation of

497 the surface image and the average displacement between the upper and lower surfaces

498 of a slice. Image volumes of each brain slice were transformed according to the resultant

499 deformation field and then stacked into the whole brain image volume. Errors of this

500 interslice stitching method were evaluated by manually recognizing 500 random pairs of

501 axonal segments cut by the vibroslicer, in the reconstructed image volume of the brain

502 hemisphere ipsilaterally injected with AAV-GFP into the MD, and calculating the average

503 shift between the ends of fibers crossing those stitched surfaces.

504 **Visualization.** The whole monkey brain image was reconstructed at 10×10×10 μm³

505 voxel resolution. The reconstruction software also supports reconstructing ROIs of user-

506 specified locations and sizes at full resolution. The image volumes of the whole brain or

507 a given ROI were converted to the Imaris file format (IMS) for visualization in Imaris

508 (v9.1~9.5, Oxford Instruments) or in our custom software, Lychnis (see below). The IMS

509 format is based on the standard hierarchical data format 5 (HDF5), which is open source

510 and supports large image data. File format conversion was performed with the Imaris

511 File Converter (v9.2, Oxford Instruments).

512 **SMART positioning system (SPS).** A positioning system was established to

513 bidirectionally map the pixels in the raw images to the reconstructed brain or ROIs. The

514 positioning system contains three spaces: (1) Raw-image space $S_1(s, k, x_r, y_r, z_r)$, where

515 the arguments represent slice (s), stack (k), frame (x_r), row (y_r), and stack (z_r) numbers

516 of a pixel in S_1; (2) Intra-slice-stitched-image space $S_2(s, x_i, y_i, z_i)$ where the arguments

517 represent the 3D position of a point (x_i, y_i, z_i) at a stitched 3D slice (s) image; (3)

518 Reconstructed-volume space $S_3(x_v, y_v, z_v)$. The coordinate mapping between spaces are

519 based on bidirectional transformations across the three spaces: (1) Resampling

520 transformation between S_1 and S_2, consisting of a set of affine transformations each

521 applied to an image stack; (2) Reconstruction transformation between S_2 and S_3,

522 consisting of a group of displacement fields each applied for a slice image. This system

523 is also extensible to the atlas space when necessary.

524

525 **Mesoscopic analysis**

526 **Fiber orientation analysis.** We visualized fiber orientation by applying structure tensor

527 analysis [45] on a low-resolution (10×10×10 μm³ voxel resolution) reconstruction of the

528 whole brain volume. The structure tensor is defined as:

529
$$ST_\rho(\nabla f) = g_\rho * (\nabla f \nabla f^T),$$

530 where ∇f is the gradient of the intensity $f(x,y,z)$, of the reconstructed 3D image. g_ρ is a

531 3D Gaussian kernel with standard deviation ρ, set as 1 pixel here.

532 Fiber orientation f_{vis} was given by the product of the secondary eigenvalue λ_2 and

533 eigenvector $\mathbf{v}_2$ of the structure tensor $ST_\rho(\nabla f)$:

534
$$(f_{vis,x}, f_{vis,y}, f_{vis,z}) = \lambda_2 \mathbf{v}_2$$

535 The resulted fiber orientation image was rendered and visualized in Imaris using the

536 *blend* mode. The *x*, *y*, and *z* components of this fiber orientation image were rendered

537 using red, green, and blue colors, respectively.

538 **Cortical flattening.** Surfaces of pial/gray (*pial*) and gray/white (*white*) boundaries were

539 reconstructed based on structural MRI images (T1 MPRAGE, 250×250×500 µm^3) of the

540 same animal using Freesurfer [46] and custom Matlab (Mathworks) scripts. The mid

541 surface between *pial* and *white* surfaces was inflated, and then 4 cuts were made to

542 flatten the surface for visualization purposes (Supplementary Fig. 10). Cortical thickness

543 was estimated by comparing *pial* and *white* surfaces. Atlas areas [47] were labeled onto

544 the flattened surface based on nonlinear co-registration between the MRI of the test

545 animal and the MRI template of the atlas, which were both nonlinearly warped to the

546 National Institute of Mental Health Macaque Template [48, 49], serving as a common

547 template. MD projection areas were determined by manually registering the coronal

548 sections from the reconstructed whole-brain image to the atlas.

549 **Parcellation.** Cortical area identification was based on manually matching the DAPI,

550 NT640 or autofluorescence images of the slices to the atlas [47] in the MIP images of each

551 slice. Cortical layers were identified from the Nissl images or cellular autofluorescence in

552 eGFP or mCherry channels.

553

Fiber tracing

We developed a software referred to as "Lychnis" for tracing axonal fibers in a 3D image block generated by multiple imaging modules, or in the whole image set generated by the SMART pipeline, in which the users can mark nodes along the axonal tracks semi-automatically.

Fiber tracing in volume blocks. A reconstructed image volume at specified ROIs generated by the reconstruction software was converted to IMS format. Using high-level HDF5 API, small image blocks of a given size, e.g. 256×256×256 pixels at user-specified resolution and location, can be loaded from the IMS file in Lychnis, taking advantage of the multi-resolution structure and chunk-wise layout of HDF5. The Visualization Toolkit (VTK) [50] and Virtual Finger technology [51, 52] are used in Lychnis for 3D rendering and interactive labeling. Semi-automatic tracing was implemented by annotating two nearby markers in the axon and the tracks were automatically extended by linear extrapolation and manual correction when necessary. The nearby image blocks were automatically loaded for continuous tracing.

When necessary, misalignment that occurred during whole-brain reconstruction between adjacent slices resulting from the imperfect automatic volume reconstruction was manually corrected by virtue of the continuity of neuronal fibers and blood vessels in Lychnis. This software provides a user interface showing 3D visualization of two adjacent slice volumes, implemented with VTK, for the users to interactively mark the breakpoints of fibers on the surfaces of both slices. Then the deformation fields of all slices could be calculated based on these markers, using the interpolation library nn [53]. Lychnis also provides bidirectional transformation between the image coordinate

577   systems before and after deformation that was also integrated in the SMART positioning

578   system.

579   **Fiber tracing in whole macaque brains.** Brain-wide axonal tracing was performed in

580   the raw-image space with an adaptive and progressive approach implemented in

581   Lychnis. All of the raw image stacks of the whole macaque brain were stored in OME-

582   TIFF format at a remote data center. Lychnis provided a dynamic mechanism for loading

583   and displaying the raw data while tracing. The starting axonal points or segments were

584   selected in the low-resolution whole brain, and their locations were mapped to the raw-

585   image coordinate system S_1 via SPS. A block of raw images centering these points was

586   loaded and assembled in memory by shifting individual images and rotating this local

587   image block for 3D visualization in the Lychnis user interface. Tracing in this image block

588   could be performed by the same semi-automatic algorithm for tracing in volumes of

589   interests. When the fiber segment in the current slice was fully traced, the SPS

590   converted the position of the last annotated point to a location in the whole-brain

591   coordinate space S_3, (x_n, y_n, z_n), and then converted the nearby point $(x_n, y_n, z_n+\varepsilon)$ back

592   to the raw-image space and loaded the corresponding image block, where ε was set to

593   make sure z_n and $z_n+\varepsilon$ located in two neighboring slices. The fibers were traced with this

594   iterative and progressive strategy block-by-block from the initial starting point or point set

595   both anterogradely along the axon tracks to their endings in all branches, or retrogradely

596   to the virus injection sites. In this study, axons from the injection site in the left

597   hemisphere labeling MD and neighboring RE areas sparsely projecting to the

598   contralateral cortical areas were traced. A few axons with significantly higher brightness

599   could also be identified and traced out from dense ipsilateral fiber bundles. After fiber

600   tracing was completed, all the points in the tracks were converted to the whole-brain

601   space S_3 for visualization. Completed tracing results were reviewed by two independent

602   annotators, and the consensus axon tracks were used for the analysis [19, 20].

603   **3D rendering.** A GPU-accelerated renderer was created and integrated into Lychnis for

604   3D rendering and creating videos. Imaris was also used for 3D rendering and creating

605   videos.

606

Acknowledgments

Author contributions

Fang Xu, L.I.Z., H.D., Fuqiang Xu, X.H., P.-M. L. and G.-Q.B. conceptualize the project. Fang Xu led this project under supervision of P.-M. L. and G.-Q.B.. Fang Xu, Y.S. and H.W. established the pipeline for whole macaque brain imaging. Fang Xu, Q.Z., H.W. and C.X. designed and set up the microscope. Y.S. performed sample preparation and acquired data. L.D. developed the software for image acquisition, visualization, and neuronal tracing. C.Y. developed the software for brain reconstruction. H.T. and X.H. injected viruses and prepared the macaques brain samples. Fang Xu, Y.S., C.Y., F.W., and R.X. analyzed the data. Q.L. developed tools for image preprocessing. P.S. and Fuqiang Xu validated and provided the tracing viruses. H.D. and R.D. provided valuable

630   neuroanatomical insights. Fang Xu, P.-M. L., and G.-Q.B. wrote the manuscript with

631   inputs from all the authors.

632

633   **Competing interests**

634   The authors have applied for a patent on the technology related to this work.

635

636   **Data and materials availability**

637   All codes used in this study are provided upon request. All data required to evaluate the

638   conclusions in the paper are present in the paper or the supplementary materials. The

639   complete imaging datasets of macaque brains exceed 1 petabyte, and therefore

640   impractical to upload to a public data repository. The subsets related to any figure or

641   video in this work are freely available upon request and providing feasible data transfer

642   mechanisms (such as physical hard disk drives, cloud storage, or onsite visiting).

643

644   **References**

645   1.   Belmonte, J.C.I. et al. Brains, Genes, and Primates. *Neuron* **86**, 617-631 (2015).
646   2.   Poo, M.-m. et al. China Brain Project: Basic Neuroscience, Brain Diseases, and Brain-
647   Inspired Computing. *Neuron* **92**, 591-596 (2016).
648   3.   Markov, N.T. et al. Cortical High-Density Counterstream Architectures. *Science* **342**,
649   1238406 (2013).
650   4.   Wang, X.-J. & Kennedy, H. Brain structure and dynamics across scales: in search of rules.
651   *Current Opinion in Neurobiology* **37**, 92-98 (2016).
652   5.   Kleinfeld, D. et al. Large-Scale Automated Histology in the Pursuit of Connectomes. *The
653   Journal of Neuroscience* **31**, 16125-16138 (2011).
654   6.   Zeng, H. Mesoscale connectomics. *Current Opinion in Neurobiology* **50**, 154-162 (2018).
655   7.   Schmahmann, J. & Pandya, D. Fiber pathways of the brain. (Oxford University Press,
656   New York, 2009).

657 8.   Lin, M.K. et al. A high-throughput neurohistological pipeline for brain-wide mesoscale
658   connectivity mapping of the common marmoset. *eLife* **8**, e40042 (2019).
659 9.   Felleman, D.J. & Van Essen, D.C. in Cereb cortex (Citeseer, 1991).
660 10. Jones, D.K., Knösche, T.R. & Turner, R. White matter integrity, fiber count, and other
661   fallacies: The do's and don'ts of diffusion MRI. *NeuroImage* **73**, 239-254 (2013).
662 11. Thomas, C. et al. Anatomical accuracy of brain connections derived from diffusion MRI
663   tractography is inherently limited. *Proceedings of the National Academy of Sciences* **111**,
664   16574-16579 (2014).
665 12. Liu, C. et al. A resource for the detailed 3D mapping of white matter pathways in the
666   marmoset brain. *Nature Neuroscience* **23**, 271-280 (2020).
667 13. Chung, K. et al. Structural and molecular interrogation of intact biological systems.
668   *Nature* **497**, 332-337 (2013).
669 14. Tomer, R., Ye, L., Hsueh, B. & Deisseroth, K. Advanced CLARITY for rapid and high-
670   resolution imaging of intact tissues. *Nature Protocols* **9**, 1682 (2014).
671 15. Zhao, S. et al. Cellular and Molecular Probing of Intact Human Organs. *Cell* **180**, 796-
672   812.e719 (2020).
673 16. Ueda, H.R. et al. Whole-Brain Profiling of Cells and Circuits in Mammals by Tissue
674   Clearing and Light-Sheet Microscopy. *Neuron* **106**, 369-387 (2020).
675 17. Susaki, E.A. et al. Whole-brain imaging with single-cell resolution using chemical
676   cocktails and computational analysis. *Cell* **157**, 726-739 (2014).
677 18. Gong, H. et al. High-throughput dual-colour precision imaging for brain-wide
678   connectome with cytoarchitectonic landmarks at the cellular level. *Nature
679   Communications* **7**, 12142 (2016).
680 19. Economo, M.N. et al. A platform for brain-wide imaging and reconstruction of individual
681   neurons. *eLife* **5**, e10566 (2016).
682 20. Winnubst, J. et al. Reconstruction of 1,000 Projection Neurons Reveals New Cell Types
683   and Organization of Long-Range Connectivity in the Mouse Brain. *Cell* **179**, 268-
684   281.e213 (2019).
685 21. Wang, Y. et al. Complete single neuron reconstruction reveals morphological diversity in
686   molecularly defined claustral and cortical neuron types. *bioRxiv*, 675280 (2019).
687 22. Wang, H. et al. Scalable volumetric imaging for ultrahigh-speed brain mapping at
688   synaptic resolution. *National Science Review* **6**, 982-992 (2019).
689 23. Bria, A. & Iannello, G. TeraStitcher - A tool for fast automatic 3D-stitching of teravoxel-
690   sized microscopy images. *BMC Bioinformatics* **13**, 316 (2012).
691 24. Hörl, D. et al. BigStitcher: reconstructing high-resolution image datasets of cleared and
692   expanded samples. *Nat Methods* **16**, 870-874 (2019).
693 25. Hayworth, K.J. et al. Ultrastructurally smooth thick partitioning and volume stitching for
694   large-scale connectomics. *Nat Methods* **12**, 319-322 (2015).
695 26. Ray, J.P. & Price, J.L. The organization of projections from the mediodorsal nucleus of
696   the thalamus to orbital and medial prefrontal cortex in macaque monkeys. *J Comp
697   Neurol* **337**, 1-31 (1993).
698 27. Parnaudeau, S., Bolkan, S.S. & Kellendonk, C. The Mediodorsal Thalamus: An Essential
699   Partner of the Prefrontal Cortex for Cognition. *Biological Psychiatry* **83**, 648-656 (2018).
700 28. Giguere, M. & Goldman-Rakic, P.S. Mediodorsal nucleus: Areal, laminar, and tangential
701   distribution of afferents and efferents in the frontal lobe of rhesus monkeys. *Journal of
702   Comparative Neurology* **277**, 195-213 (1988).

29. Friedman, D.P. & Murray, E.A. Thalamic connectivity of the second somatosensory area and neighboring somatosensory fields of the lateral sulcus of the macaque. *Journal of Comparative Neurology* **252**, 348-373 (1986).

30. Gao, R. et al. Cortical column and whole-brain imaging with molecular contrast and nanoscale resolution. *Science* **363**, eaau8302 (2019).

31. Bria, A., Iannello, G., Onofri, L. & Peng, H. TeraFly: real-time three-dimensional visualization and annotation of terabytes of multidimensional volumetric images. *Nat Methods* **13**, 192-194 (2016).

32. Wang, Y. et al. TeraVR empowers precise reconstruction of complete 3-D neuronal morphology in the whole brain. *Nature Communications* **10**, 3474 (2019).

33. Luo, L., Callaway, E.M. & Svoboda, K. Genetic Dissection of Neural Circuits: A Decade of Progress. *Neuron* **98**, 256-281 (2018).

34. Lin, R. et al. Cell-type-specific and projection-specific brain-wide reconstruction of single neurons. *Nature Methods* **15**, 1033-1036 (2018).

35. Friedmann, D. et al. Mapping mesoscale axonal projections in the mouse brain using a 3D convolutional network. *Proceedings of the National Academy of Sciences* **117**, 11068-11075 (2020).

36. Glasser, M.F. et al. A multi-modal parcellation of human cerebral cortex. *Nature* **536**, 171-178 (2016).

37. Levinthal, D.J. & Strick, P.L. Multiple areas of the cerebral cortex influence the stomach. *Proceedings of the National Academy of Sciences* **117**, 13078-13083 (2020).

38. Jungmann, A., Leuchs, B., Rommelaere, J., Katus, H.A. & Müller, O.J. Protocol for efficient generation and characterization of adeno-associated viral vectors. *Human gene therapy methods* **28**, 235-246 (2017).

39. Wu, S.H. et al. Comparative study of the transfection efficiency of commonly used viral vectors in rhesus monkey (Macaca mulatta) brains. *Zool Res* **38**, 88-95 (2017).

40. Jing, W. et al. A new MRI approach for accurately implanting microelectrodes into deep brain structures of the rhesus monkey (Macaca mulatta). *Journal of Neuroscience Methods* **193**, 203-209 (2010).

41. Linkert, M. et al. Metadata matters: access to image data in the real world. *The Journal of cell biology* **189**, 777-782 (2010).

42. Goldberg, I.G. et al. The Open Microscopy Environment (OME) Data Model and XML file: open tools for informatics and quantitative analysis in biological imaging. *Genome biology* **6**, R47 (2005).

43. Ziv, J. & Lempel, A. Compression of individual sequences via variable-rate coding. *IEEE transactions on Information Theory* **24**, 530-536 (1978).

44. Welch, T.A. A technique for high-performance data compression. *Computer*, 8-19 (1984).

45. Schilling, K.G. et al. Histological validation of diffusion MRI fiber orientation distributions and dispersion. *Neuroimage* **165**, 200-221 (2018).

46. Fischl, B. FreeSurfer. *Neuroimage* **62**, 774-781 (2012).

47. Saleem, K.S. & Logothetis, N.K. A combined MRI and histology atlas of the rhesus monkey brain in stereotaxic coordinates. (Academic Press, 2012).

48. Van Essen, D.C., Glasser, M.F., Dierker, D.L. & Harwell, J. Cortical Parcellations of the Macaque Monkey Analyzed on Surface-Based Atlases. *Cerebral Cortex* **22**, 2227-2240 (2011).

49. Seidlitz, J. et al. A population MRI brain template and analysis tools for the macaque. *Neuroimage* **170**, 121-131 (2018).

751   50.   Schroeder, W.J., Lorensen, B. & Martin, K. The visualization toolkit: an object-oriented
752   approach to 3D graphics. (Kitware, 2004).
753   51.   Peng, H. et al. Virtual finger boosts three-dimensional imaging and microsurgery as well
754   as terabyte volume image visualization and analysis. *Nature communications* **5**, 4342
755   (2014).
756   52.   Peng, H., Bria, A., Zhou, Z., Iannello, G. & Long, F. Extensible visualization and analysis
757   for multidimensional images using Vaa3D. *Nature Protocols* **9**, 193 (2014).
758   53.   Fan, Q., Efrat, A., Koltun, V., Krishnan, S. & Venkatasubramanian, S. in ALENEX/ANALCO
759   111-120 (2005).

760   54.   Morphological data of 8 mouse MD neurons and 2 RE neurons were from the
761   MouseLight project. Neuron IDs: AA0054 (DOI: 10.25378/janelia.5521765), AA0055
762   (DOI: 10.25378/janelia.5521768), AA0094 (DOI: 10.25378/janelia.5526661), AA0095
763   (DOI: 10.25378/janelia.5526664), AA0138 (DOI: 10.25378/janelia.5527288), AA0353
764   (DOI: 10.25378/janelia.5526664), AA0363 (DOI: 10.25378/janelia.7613897), AA0368
765   (DOI: 10.25378/janelia.7613912), AA0370 (DOI: 10.25378/janelia.7613921) and AA0371
766   (DOI: 10.25378/janelia.7613924).

767 **Figures**
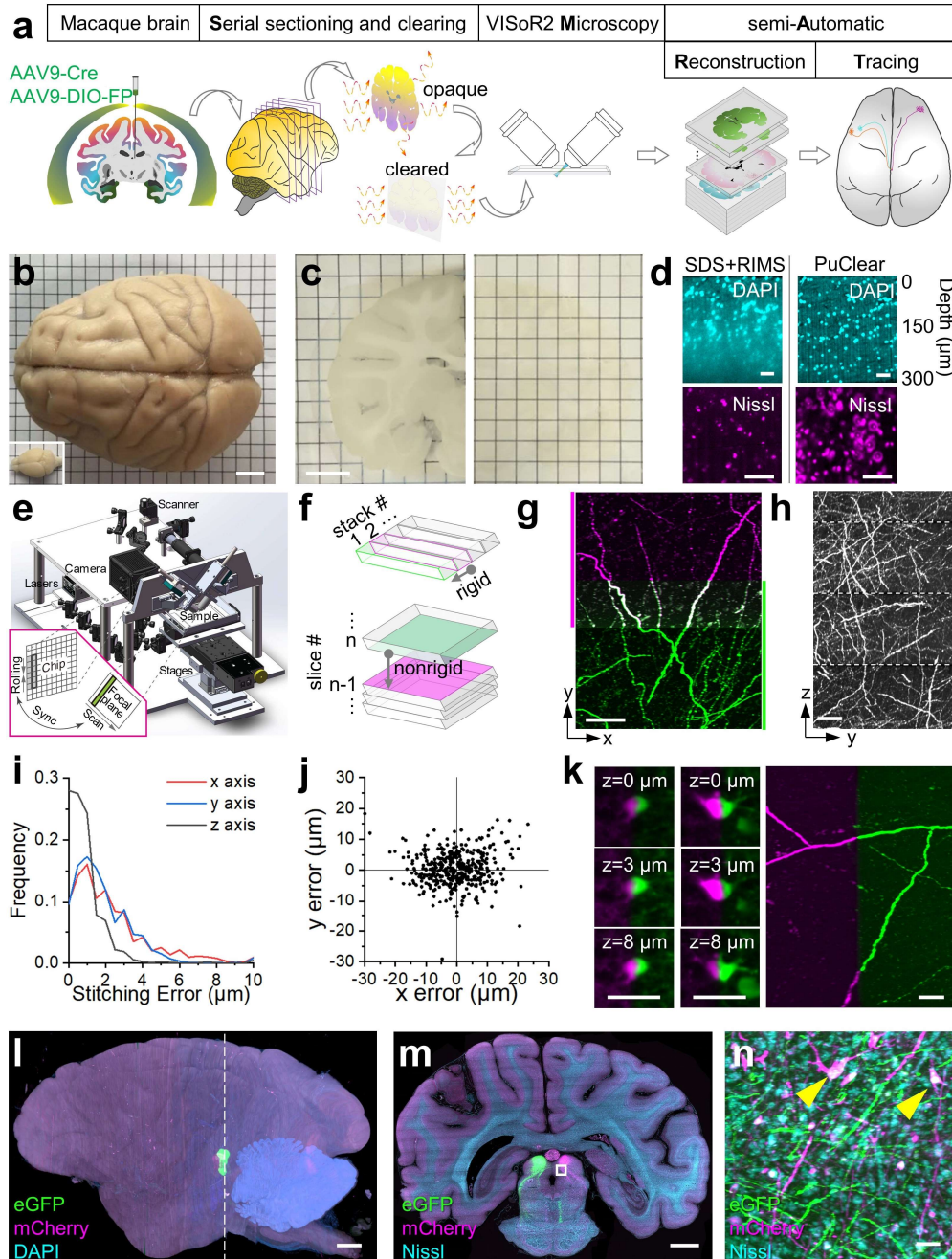
768

769 **Fig. 1 | The SMART approach for high-throughput mapping of a rhesus macaque**

770 **brain at micron resolution.** (**a**) The SMART pipeline. (**b**) A macaque brain compared

771 with a mouse brain (bottom left). (**c**) A macaque brain slice before (left) and after (right;

772 flipped) PuClear treatment. (**d**) Comparison between SDS- and RIMS-based clearing,

773   and PuClear treatment. Top panels: WM areas stained with DAPI. Bottom panels:

774   cortical areas stained with a fluorescent Nissl dye, NT640. (**e**) The VISoR2 imaging

775   system. Inset: a schematic showing the synchronization mechanism between laser

776   scanning and camera readout. (**f**) A schematic for volume stitching within a single slice

777   (top) and between slices (bottom). (**g**) Maximum intensity projection (MIP) image of a

778   100-µm coronal section of two adjacent stacks (separately color-coded) with merged

779   overlapped regions after stitching. (**h**) MIP of a 50-µm virtual section from 4 consecutive

780   slices. (**i-j**) Distributions of the errors of intra-slice (i) and inter-slice (j) stitching. (**k**)

781   Stitched neurons (each shown in 3 z-sections) and axonal branches cut into two

782   adjacent brain slices (separately color-coded). (**l**) A reconstructed macaque brain with

783   viral labeling of bilateral SC areas. (**m**) MIP of a 30-µm coronal section indicated with a

784   dashed line in (l). (**n**) Magnified view of the boxed region in (m). Arrowheads indicate

785   neurons co-labeled by the virus and fluorescent Nissl staining. Scale bars: (b), (c), 10

786   mm; (d), (k) and (n), 50 µm; (g-h), 100 µm; (l) and (m), 5 mm.

787
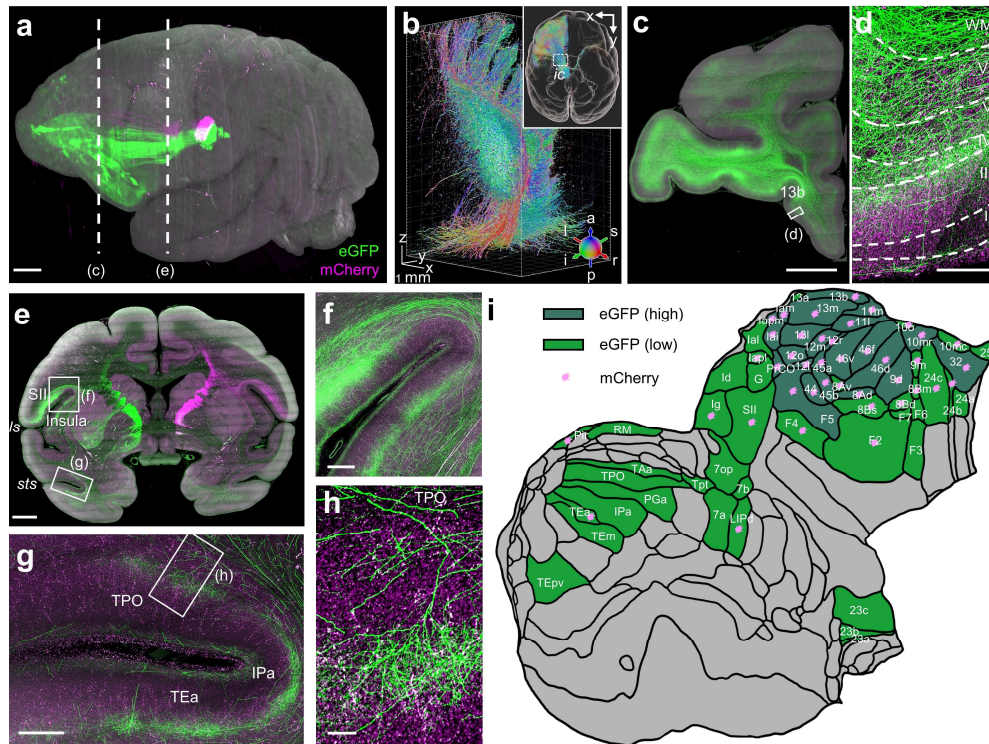
Fig. 2 | Mesoscopic mapping of the MD projection. (**a**) A reconstructed macaque brain with viral labeling of bilateral MD areas. (**b**) Fiber orientation image of the brain (inset) and a magnified view of the left *ic* (box region). Only the eGFP channel is displayed, where red, green, and blue colors represent the right/left, anterior/posterior, and superior/inferior orientations, respectively. (**c-h**) MIPs of two 300-μm coronal sections (c, e), and the magnified views (d, f, g, h) of the boxed regions specified in (c), (e), and (g). Cortical layers were drawn based on the autofluorescence patterns in each channel. (**i**) Summarized cortical flat map showing high- and low-density distribution of axonal projections to the ipsilateral hemisphere from the injection sites revealed by eGFP and mCherry expression. Scale bars: (a), (c), (e), 5 mm; (d), (g), 500 μm; (f), 1 mm; (h), 100 μm. Green codes the eGFP channel and magenta codes the mCherry channel in all panels except in (b). Acronyms: *ic*, internal capsule; *ls*, lateral sulcus; *sts*, superior temporal sulcus; others are listed in Supplementary Table 1.
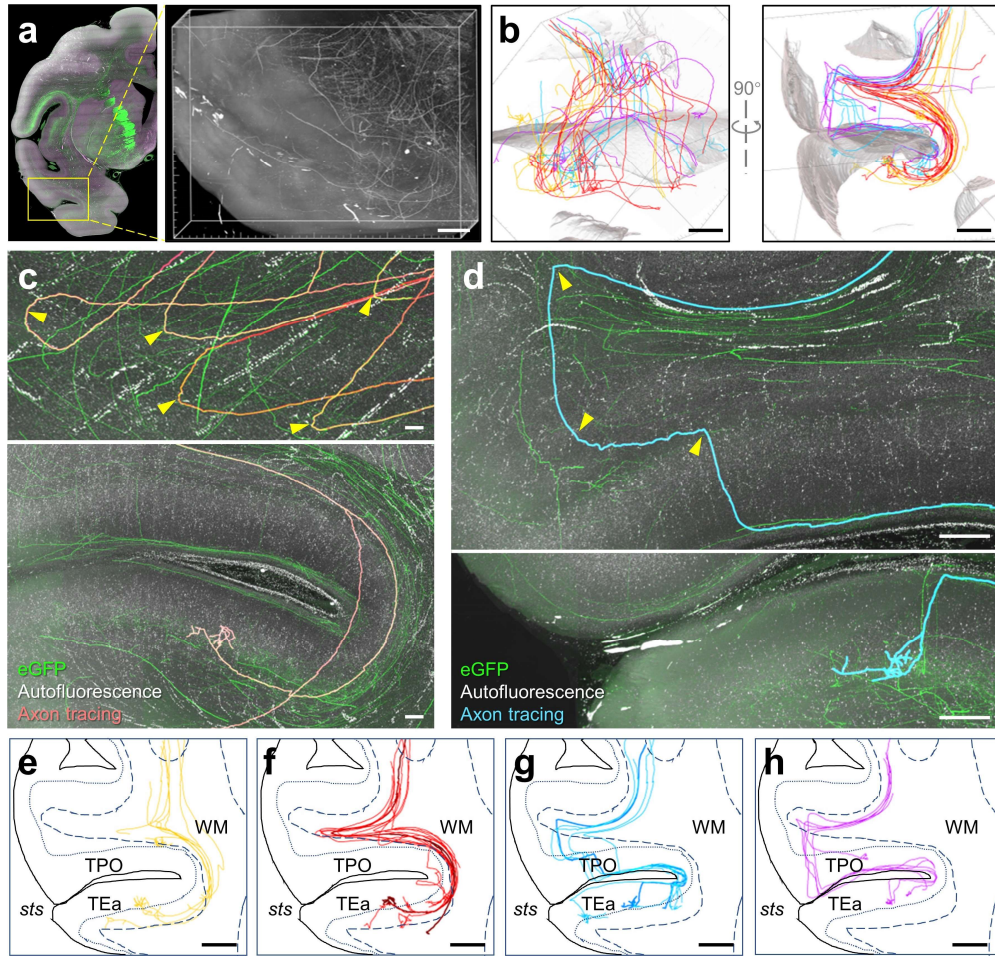
Fig. 3 | Organization of axonal fibers in cortical folds. (**a**) Overview of a 16×11×11 mm^3 image volume surrounding the *sts* from an MD-injected macaque. (**b**) 30 traced axonal segments shown from two perspectives. Curved brain surfaces were segmented and rendered as a shaded reference to help visualize the location of axon trajectories. (**c**) Example images showing the sharp turns (arrowheads) of 5 axons (top) in the white matter (WM) and the arbor area of an axon (bottom). (**d**) Example images showing the right-angle turns (arrowheads) of an axon (top) and its arbors (bottom). Images in the top panels of (c) and (d) are MIPs of 450-μm virtual sections resliced in an orientation parallel to the fibers. The bottom images are MIPs of 1200-μm sections. (**e-h**) Four axonal navigation patterns, including: those following short paths (e), those making sharp turns (f), those making two-step right-angle turns (g), and those making right-angle turns (h). The boundaries of cortical surfaces are illustrated as solid lines; boundaries of the WM are illustrated as dashed lines. Cortical layer IV can be recognized as a dim band in the autofluorescence images; it is drawn with dotted lines. Fibers shown in (c)

818   and (d) are highlighted in (f) and (g), respectively. Scale bars: (a-b), (e-h), 2 mm; (c) and

819   (d), 200 µm. Acronyms: *sts*, superior temporal sulcus; TPO, *sts* dorsal bank area; TEa,

820   *sts* ventral bank area; WM, white matter.

821

822
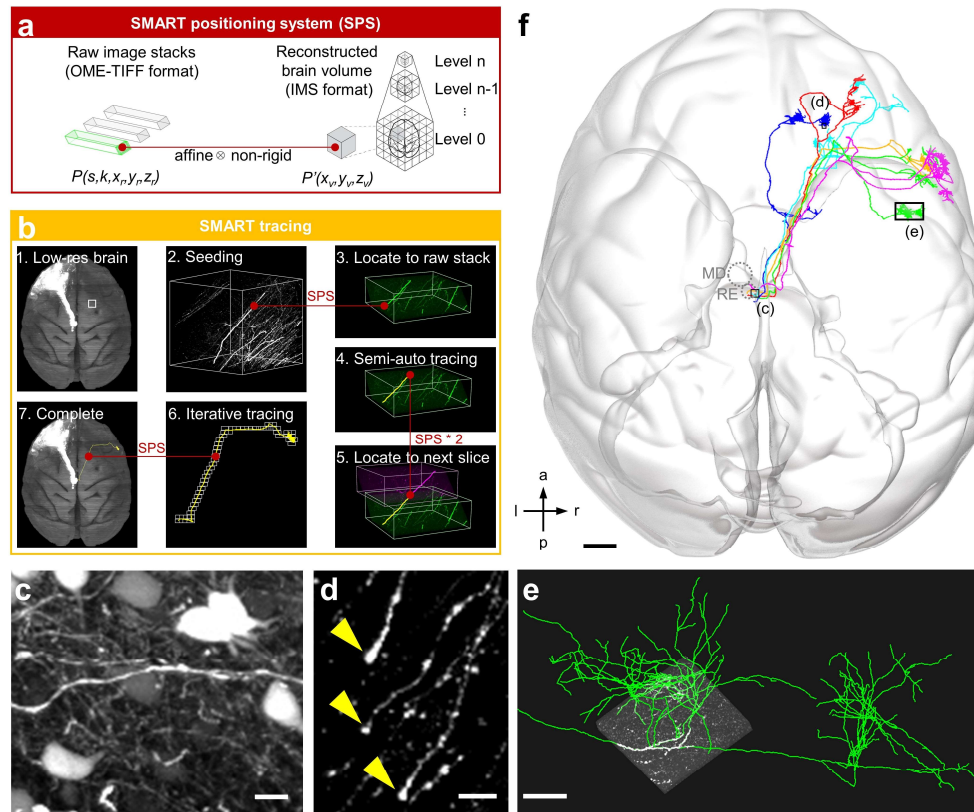
Fig. 4 | Brain-wide tracing of axonal projections. (a) The SMART positioning system (SPS) maps between any position (x_r, y_r, z_r) in the raw image stack (k) of a brain slice (s) and the corresponding point (x_v, y_v, z_v) in the space of the reconstructed brain volume. (**b**) Step-by-step workflow for SMART-based axonal tracing. Starting from a low-resolution image (b1), a seed node was selected (b2) and located via SPS in the raw image stack (b3); subsequent semi-automated tracing was conducted (b4) to navigate through to the edge of the slice and beyond into the neighboring zone of the adjacent slice as identified by SPS (b5). The entire axon can then be traced by iteratively applying steps 4 and 5 (b6), and finally visualized in the reconstructed brain space by reverse transformation of traced coordinates via SPS (b7). (**c-d**) Tracing was terminated at the injection site where the axons were too dense (c) or at axonal termini (d). (**e**) Magnified view of axonal terminals overlapped with a raw image block. (**f**) Six thalamocortical axons projecting to the right hemisphere from the left MD or RE areas are shown. Scale bars: (c), 20 μm; (d), 10 μm; (e), 500 μm; (f), 5 mm. Acronyms: MD, mediodorsal nucleus; RE, reunions nucleus.

a

Macaque brain	**S**erial sectioning and clearing	VISoR2 **M**icroscopy	semi-**A**utomatic	
			Reconstruction	**T**racing

AAV9-Cre
AAV9-DIO-FP

opaque

cleared

b

c

d SDS+RIMS | PuClear

DAPI | DAPI

Depth (μm)

0

150

300

Nissl | Nissl

e

Scanner

Camera

Lasers

Sample

Stages

Rolling

Chip

Sync

Focal plane

Scan

f

stack #
1 2 ...

rigid

slice #

n

n-1

nonrigid

g

y

x

h

z

y

i

Frequency

0.3

0.2

0.1

0.0

0   2   4   6   8   10

Stitching Error (μm)

— x axis
— y axis
— z axis

j

y error (μm)

30

20

10

0

-10

-20

-30

-30 -20 -10 0 10 20 30

x error (μm)

k

z=0 μm | z=0 μm

z=3 μm | z=3 μm

z=8 μm | z=8 μm

l

eGFP
mCherry
DAPI

m

eGFP
mCherry
Nissl

n

eGFP
mCherry
Nissl

a

eGFP
mCherry

(c) (e)

b

x
y
ic

z
x y
1 mm

a
s
i
r
p
l

c

13b
(d)

d

WM
VI
V
IV
III
II
I

e

SII (f)
Insula
ls
sts (g)

f

g

TPO
(h)
IPa
TEa

h

TPO

i

eGFP (high)
eGFP (low)
mCherry

13a 13b
Iam 13m
Iapm 11m
Ial 11l
Iapl 13l 12r 46f 10o
Id 12o 46v 46d 10mr 10mc
Ig PrCO 12l 45a 9m 32 25
SII 44 3Av 9d 24c
F4 45b 8Ad 3Bd 24b
F5 8BS E7 F6 24b
Pir RM F2 F3
TPO TAa 7op Tpt
TEa IPa PGa 7b
TEm 7a LIPd
TEpv
23c
23b
23a

a

b

c

eGFP
Autofluorescence
Axon tracing

d

eGFP
Autofluorescence
Axon tracing

e

WM

TPO

TEa

sts

f

WM

TPO

TEa

sts

g

WM

TPO

TEa

sts

h

WM

TPO

TEa

sts

a SMART positioning system (SPS)

Raw image stacks (OME-TIFF format) → Reconstructed brain volume (IMS format)

Level n
Level n-1
Level 0

affine ⊗ non-rigid

$P(s, k, x_r, y_r, z_r)$ $P'(x_v, y_v, z_v)$

b SMART tracing

1. Low-res brain
2. Seeding
3. Locate to raw stack — SPS
4. Semi-auto tracing
5. Locate to next slice — SPS * 2
6. Iterative tracing — SPS
7. Complete

f

(d)

MD
RE
(c)

(e)

a
l — r
p

c

d

e